

# PAGANI Toolkit: Parallel graph-theoretical analysis package for brain network big data

Haixiao Du<sup>1</sup> | Mingrui Xia<sup>2,3,4</sup>  | Kang Zhao<sup>1</sup> | Xuhong Liao<sup>2,3,4</sup> |  
Huazhong Yang<sup>1</sup> | Yu Wang<sup>1</sup> | Yong He<sup>2,3,4</sup> 

<sup>1</sup>Department of Electronic Engineering, Tsinghua University, Beijing, China

<sup>2</sup>National Key Laboratory of Cognitive Neuroscience and Learning, Beijing Normal University, Beijing, China

<sup>3</sup>Beijing Key Laboratory of Brain Imaging and Connectomics, Beijing Normal University, Beijing, China

<sup>4</sup>IDG/McGovern Institute for Brain Research, Beijing Normal University, Beijing, China

## Correspondence

Yu Wang, PhD, Department of Electronic Engineering, Tsinghua University, Beijing 100084, China.

Email: yu-wang@tsinghua.edu.cn  
and

Yong He, PhD, National Key Laboratory of Cognitive Neuroscience and Learning, Beijing Key Laboratory of Brain Imaging and Connectomics, IDG/McGovern Institute for Brain Research, Beijing Normal University, Beijing 100875, China.  
Email: yong.he@bnu.edu.cn

## Funding information

Natural Science Foundation of China, Grant/Award Numbers: 81401479, 81671767, 81620108016, 31521063, 61622403, 61621091; Beijing Natural Science Foundation, Grant/Award Numbers: Z161100004916027, Z151100003915082, Z161100000216152, Z161100000216125; Fundamental Research Funds for the Central Universities, Grant/Award Numbers: 2015KJCA13, 2017XTCX04; Changjiang Scholar Professorship Award, Grant/Award Number: T2015027

## Abstract

The recent collection of unprecedented quantities of neuroimaging data with high spatial resolution has led to brain network big data. However, a toolkit for fast and scalable computational solutions is still lacking. Here, we developed the PArallel Graph-theoretical ANALYSIS (PAGANI) Toolkit based on a hybrid central processing unit–graphics processing unit (CPU–GPU) framework with a graphical user interface to facilitate the mapping and characterization of high-resolution brain networks. Specifically, the toolkit provides flexible parameters for users to customize computations of graph metrics in brain network analyses. As an empirical example, the PAGANI Toolkit was applied to individual voxel-based brain networks with ~200,000 nodes that were derived from a resting-state fMRI dataset of 624 healthy young adults from the Human Connectome Project. Using a personal computer, this toolbox completed all computations in ~27 h for one subject, which is markedly less than the 118 h required with a single-thread implementation. The voxel-based functional brain networks exhibited prominent small-world characteristics and densely connected hubs, which were mainly located in the medial and lateral fronto-parietal cortices. Moreover, the female group had significantly higher modularity and nodal betweenness centrality mainly in the medial/lateral fronto-parietal and occipital cortices than the male group. Significant correlations between the intelligence quotient and nodal metrics were also observed in several frontal regions. Collectively, the PAGANI Toolkit shows high computational performance and good scalability for analyzing connectome big data and provides a friendly interface without the complicated configuration of computing environments, thereby facilitating high-resolution connectomics research in health and disease.

## KEYWORDS

Big Data, connectome, CUDA, fMRI, graph theory, hub

## 1 | INTRODUCTION

The human brain is organized as a complex network comprising numerous interacting neuronal elements. Recent developments in noninvasive magnetic resonance imaging technologies and graph theoretical approaches have provided a promising framework for characterizing

the topological properties of complex brain networks, that is, connectomics (Sporns, Tononi, & Kotter, 2005). Based on the imaging connectomics framework, researchers have revealed many important topological characteristics of healthy human brain networks, including the small-world properties, modular structure, and densely connected hubs (Bullmore & Sporns, 2012; Liao, Vasilakos, & He, 2017; Sporns & Betzel, 2016; van den Heuvel & Sporns, 2013). Moreover, imaging connectomics have been widely used to study topological changes in brain

Haixiao Du, Mingrui Xia and Kang Zhao contributed equally to this work.

networks during development (Cao, Huang, & He, 2017; Cao et al., 2017; Keunen, Counsell, & Benders, 2017) and aging (Ferreira et al., 2016; Grayson & Fair, 2017; Zuo et al., 2017) and in neuropsychiatric disorders (Fornito, Zalesky, & Breakspear, 2015; Stam, 2014; Xia & He, 2011).

The construction of brain networks has typically been confined to a coarse level based on regions of interest (ROIs) derived from various anatomically and functionally predefined parcellation atlases (Cohen et al., 2008; Fan et al., 2016; Glasser et al., 2016; Power et al., 2011; Tzourio-Mazoyer et al., 2002). These atlas-based studies have provided substantial knowledge regarding the organization of the brain from a macroscopic perspective. However, atlas-based studies employ a variety of different *priori* parcellation schemes and typically ignore spatial inhomogeneity within large ROIs (Jiang et al., 2015), which may bias the results and conclusions. Moreover, inspired by technical advances, the research community has contributed enormous quantities of connectomics data, referred to as “Big Data” (Xia & He, 2017), at unprecedented rates, such as the Human Connectome Project (HCP) (Van Essen et al., 2012). Growing datasets with higher resolution have provided a large amount of novel information with finer details that can be better used to explore the functional architecture of human brain networks (Castellanos, Di Martino, Craddock, Mehta, & Milham, 2013; Xia & He, 2017). However, although the Big Data research model represents a highly promising research direction, it also requires breakthrough algorithmic and computational solutions. Thus, fast and efficient computational tools scalable to brain network big data are urgently required.

Several publicly available toolboxes, such as the Brain Connectivity Toolbox (BCT) (Rubinov & Sporns, 2010), Graph-Analysis Toolbox (GAT) (Hosseini, Hoefl, & Kesler, 2012), and GRaph thEoreticAl Network Analysis toolbox (GRETNA) (Wang et al., 2015), have facilitated imaging connectomics studies by utilizing graph theoretical network analysis approaches. However, these popular toolboxes have difficulties dealing with brain network big data of large network sizes. Recent advances in graphics processing units (GPUs) have provided promising solutions to the high computational requirements. Over the past decade, GPUs have been used for fast graphic processing and other general-purpose parallel computations in the domain of neuroimaging (Eklund, Dufort, Forsberg, & LaConte, 2013; Wang et al., 2013); however, these advances are rarely utilized in the topological analysis of human brain networks because they lack automatic and flexible software based on GPUs to fulfill the urgent requirements for the analysis of brain network big data.

Here, based on a CPU-GPU hybrid framework, we developed a PArallel Graph-theoretical ANALysis (PAGANI) Toolkit that can quickly compute the global and nodal topological characteristics of large brain networks. The toolkit incorporates a user-friendly interface and low requirements of the computing environment. We further comprehensively evaluated the performance of the PAGANI Toolkit for different network sizes and densities. The results demonstrated that this advanced toolbox can substantially reduce the time consumption and improve the clinical applicability for mapping high-resolution brain networks from big data. Moreover, we illustrated the application of the PAGANI Toolkit using a resting-state fMRI (R-fMRI) dataset from the

HCP, which contains 873 subjects under the original 2-mm (isotropic) resolution. We further examined the gender-related differences in both global and nodal metrics of the high-resolution functional networks and characterized the relationship between these network metrics and individual cognitive abilities (intelligence quotient and emotion recognition score).

## 2 | MATERIALS AND METHODS

### 2.1 | Overview of functionality of the PAGANI toolkit

The PAGANI Toolkit was developed in a hybrid CPU-GPU framework with C/C++ and CUDA (Computing Unified Device Architecture) as programming languages and QT as a GUI designing software under a 64-bit Microsoft Windows environment and the General Public License (GPL). The PAGANI Toolkit is an open-source software package containing background computation and the GUI as two separate modules. The computation module was developed based on a previously described CPU-GPU accelerated framework (Wang et al., 2013) packaged into independent executable files for different functions. The well-designed GUI module can flexibly generate scripts to call executable commands to perform batch computations.

The greatest advantage of the PAGANI Toolkit compared with the existing connectomics-related toolboxes (e.g., BCT, GRETNA and GAT) is the implementation of a fast and scalable technique to construct voxel-wise functional brain networks from preprocessed high-resolution fMRI data and to calculate graph-based global and nodal metrics of networks derived from any species or imaging data modality (Table 1). Some graph-based toolboxes, such as GRETNA, take advantages of parallel computing with multicore CPUs to accelerate analyses of a large quantity of ROI-defined networks by calculating subjects' connectomes concurrently. However, the between-subject parallel model is inefficient for large voxel-wise networks because it requires the maintenance of all connectivity matrices of every subject in memory. To address this issue, the PAGANI Toolkit parallelizes graph-based computations at a finer granularity, node, and edge level concurrently within an individual network, by employing a hybrid CPU-GPU framework. The toolbox also uses a sparse data structure to store the voxel-wise network to improve the scalability of the software platform.

As illustrated in Figure 1, calculation of the network topological metrics in the PAGANI Toolkit can be categorized into two levels, the global and nodal levels (for detailed definitions, see Supporting Information, Table S1), and the calculation dependencies are as follows. Computations of  $C_p$  and  $L_p$  depend on calculation of the nodal clustering coefficient and nodal efficiency, respectively. Computation of the all-pairs shortest path (APSP) precedes nodal efficiency calculation. The results of the modular detection are required for the computation of participation coefficients. GPUs are used to accelerate functional network construction and computations of various network metrics with high parallelism, including the characteristic shortest path length, eigenvector-based module detection (Newman, 2006), nodal efficiency, betweenness, and eigenvector centrality. Other computations are implemented on single or multicore CPUs, including heuristic Louvain module

TABLE 1 Summary of neuroscience connectomics tools

Software	R-fMRI preprocessing	Network construction	Graph analysis	GUI	Vis	Parallel computing	High-resolution network analysis
PAGANI	×	√	√	√	×	√	√
GRETNA (Wang et al., 2015)	√	√	√	√	×	√	×
BCT (Rubinov & Sporns, 2010)	×	×	√	×	×	×	×
GAT (Hosseini et al., 2012)	×	√	√	√	√	×	×
CONN (Whitfieldgabrieli & Nietocastanon, 2012)	√	√	√	√	√	×	×
eConnectome (He et al., 2011)	×	√	×	√	√	×	×
GraphVar (Kruschwitz, List, Waller, Rubinov, & Walter, 2015)	×	√	√	√	√	×	×

Note. Abbreviations: GUI, graphical user interface; Vis, visualization.

detection (Blondel, Guillaume, Lambiotte, & Lefebvre, 2008), global and nodal clustering coefficient, nodal degree and participation coefficient.

The GUI (Figure 2) of the PAGANI Toolkit enables customized computations in the network analysis. Global and nodal metrics are separated into two panels in the GUI. Tooltips and item information for each function and parameter are displayed when the mouse is hovered over the items. An operation manual is included in the package to provide detailed instructions for using the PAGANI Toolkit via either the GUI or the command line.

## 2.2 | Network type

The current version of the PAGANI Toolkit supports the analysis of both binary and weighted networks. The connectivity matrix is defined as  $C = [c_{ij}]$ , where  $c_{ij}$  is a non-negative connectivity strength value that quantifies the internode similarity. For example,  $C$  can be derived from a correlation matrix by setting negative correlations as either zeros or

their absolute values. The binary network is defined as an adjacency matrix  $A = [a_{ij}]$ ,

$$a_{ij} = \begin{cases} 1, & \text{if } c_{ij} > \hat{r}; \\ 0, & \text{others} \end{cases}$$

and the weighted network  $W = [w_{ij}]$  is defined as

$$w_{ij} = \begin{cases} c_{ij}, & \text{if } c_{ij} > \hat{r}; \\ 0, & \text{others} \end{cases}$$

Where  $\hat{r}$  is a connectivity strength threshold. Notably,  $\hat{r}$  is constant in the thresholding strategy using connectivity strength across different subjects. However, for density thresholding,  $\hat{r}$  is subject-specific and determined by the given network density.

## 2.3 | Global network properties

The PAGANI Toolkit is available for the computation of several popular global network properties, including the clustering coefficient ( $C_p$ ), the

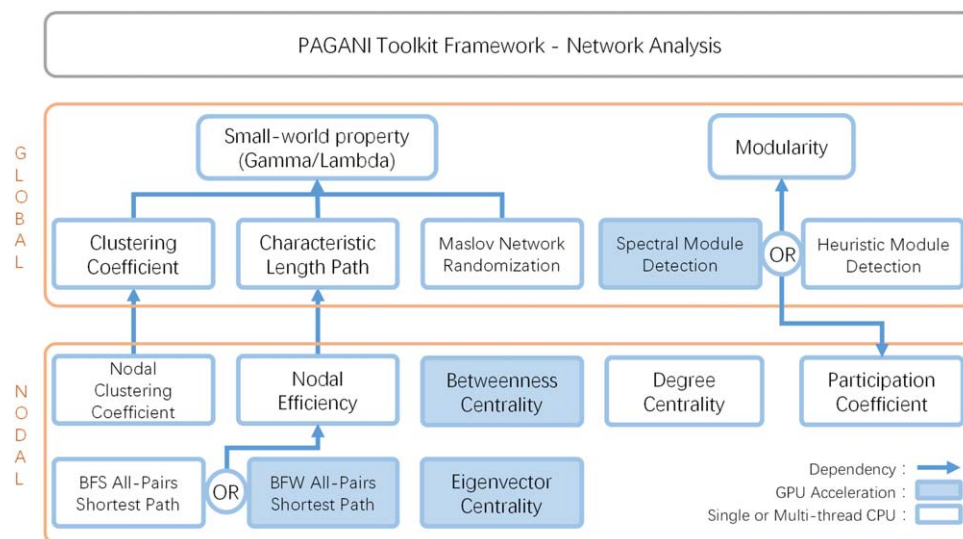
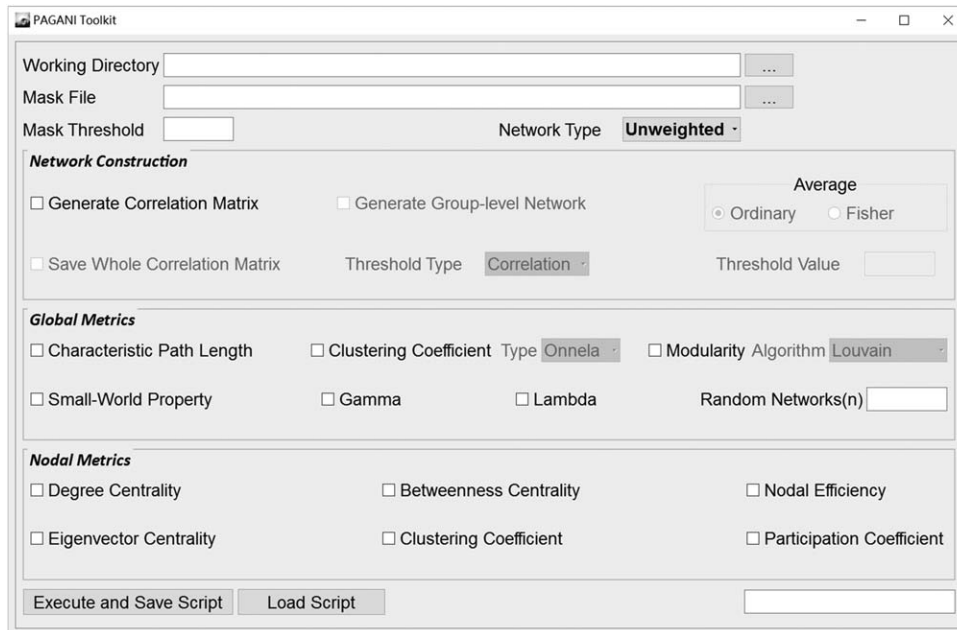


FIGURE 1 Overview of the PAGANI Toolkit. Blue items are accelerated on GPU devices in the PAGANI Toolkit [Color figure can be viewed at [wileyonlinelibrary.com](http://wileyonlinelibrary.com)]



**FIGURE 2** Graphical user interface (GUI) of the PAGANI Toolkit. Users can customize the parameter settings through the GUI

normalized clustering coefficient (Gamma, i.e.,  $C_p/C_{p_{rand}}$ ), the characteristic shortest path length ( $L_p$ ), the normalized characteristic length (Lambda, i.e.,  $L_p/L_{p_{rand}}$ ), small-worldness (Sigma, i.e.,  $\text{Gamma}/\text{Lambda}$ ), and modularity (Rubinov & Sporns, 2010).  $C_{p_{rand}}$  and  $L_{p_{rand}}$  refer to the average  $C_p$  and  $L_p$  of several surrogate random networks, the number of which can be customized in the GUI panel. The computations of  $C_p$  and  $L_p$ , and the generation of random networks are the basic functionalities required. For details regarding these network parameters, see below.

### 2.3.1 | Computation of $C_p$ and $L_p$

For a given network, its  $C_p$  is defined as the average across the nodal clustering coefficient of all voxels. The  $L_p$  of a network is defined as the “harmonic mean” shortest path length among all potential pairs of nodes, which is the reciprocal of the average nodal efficiency. Using the harmonic mean instead of the arithmetic mean is more satisfactory when disconnected components exist in a network (Newman, 2003; Wang et al., 2015) (Supporting Information, Table S1). Users are free to select the output of each nodal and global metric via the GUI.

In PAGANI, the CPU-based parallel acceleration for  $C_p$  and nodal metrics was designed to evenly assign the computation to all CPU cores at the nodal level within an individual brain network instead of the subject-level parallelism utilized in other existing toolboxes (Wang et al., 2015). Processing multiple subjects in parallel requires maintenance of the network matrices of these subjects in the memory concurrently, which is not adaptable to large voxel-wise brain networks. Moreover, the PAGANI Toolkit provides two algorithms to the calculate weighted  $C_p$  (for the formulas, see Supporting Information, Table S1) (Barrat, Barthelemy, Pastor-Satorras, & Vespignani, 2004; Onnela, Saramaki, Kertesz, & Kaski, 2005). There are no differences in memory requirements and theoretical time complexity between these two algorithms. However, the  $C_p$  algorithm from Onnela et al. (2005) takes

more time because it requires computation of the cube root, which is slower than simple multiplication and addition.

For  $L_p$  and nodal efficiency calculations, both the breadth-first search (BFS) algorithm and the blocked Floyd–Warshall’s (BFW) algorithm are implemented to calculate APSP. The BFS algorithm is implemented by a multicore CPU and performs well in sparse graphs, whereas the GPU-based BFW algorithm is more efficient for dense networks. The BFS algorithm launches a small number of threads, and each thread computes the efficiency of a subset of nodes sequentially. A distance vector (a single row of a pairwise distance matrix) indicating the shortest path length between a current node and all other nodes in a network can be reutilized within a thread. Therefore, the BFS algorithm only needs to store a sparse graph and a few distance vectors and uses less memory than the BFW algorithm which requires maintenance of the entire distance matrix in memory. For detailed applications of the two APSP algorithms, please refer to our previous work (Wang et al., 2013).

The PAGANI Toolkit currently implements the automatic selection of these algorithms for binary networks based on a lookup table (LUT) method. The lookup table is predefined in the PAGANI Toolkit with time consumptions for executing BFS and BFW algorithms for a large range of network sizes with different densities. Given a particular network, the program estimates the time consumption of the two algorithms based on the predefined LUT and automatically selects an algorithm. Only the BFW algorithm is available for weighted networks in the current version of PAGANI.

### 2.3.2 | Generation of random networks

Random networks are generated by a random rewiring process (Maslov & Sneppen, 2002), in which the number of nodes and edges and the distribution of the nodal degree remain the same as the original brain network. Initially, the process randomly selects two edges ( $V_1, V_2$ ) and

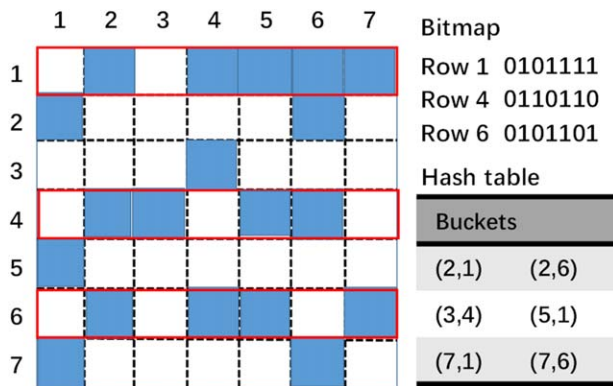


**FIGURE 3** A schematic of the data structure combining a bitmap and a hash table. The dense rows were stored in a bitmap, while the sparse rows were stored in a hash table. The determination of whether a row is stored in a bitmap or a hash table optimizes the memory usage [Color figure can be viewed at [wileyonlinelibrary.com](http://wileyonlinelibrary.com)]

(V3, V4), where node V1 connects to node V2 and node V3 connects to node V4. Subsequently, the original edges are replaced with (V1, V3) and (V2, V4) if the new edges do not exist in the original network. This procedure is typically repeated for twice the number of edges in the reference network. The graph frequently updates, removing and inserting the edges in the iterative rewiring process. Therefore, the network randomization can be regarded as a dynamically changing graph problem.

To efficiently store and update dynamically changing graphs, we adopted a novel data representation based on the combination of a bitmap and a hash table (Figure 3). Specifically, we maintained a bitmap only for dense rows in the adjacency matrix instead of storing the entire matrix. The storage for each row in the bitmap requests  $n/8$  bytes, where  $n$  is the number of nodes. Sparse rows are stored in a data structure based on the hash table proposed by Que, Checconi, Petrini, & Gunnels (2015). This hash table requires  $8 * m_i / l$  bytes for the storage of  $m_i$  connections related to the  $i$ -th node (i.e.,  $m_i$  nonzero entries in  $i$ -th row in the adjacency matrix). Each connection requires 8 bytes to store the indices of two end nodes, and  $l$  is the load factor describing the ratio of the number of stored elements in the hash table to the actual allocated memory space of the hash table. Notably, less harsh conflicts occur with decreasing load factors. Here, we empirically set the load factor to 1/2. We can easily obtain an optimal strategy that minimizes the memory usage with rows containing more than  $l * n / 64$  nonzero entries stored in the bitmap and otherwise stored in the hash table. The hash table is hashed on edges utilizing a Fibonacci function. Please refer to Que et al. (2015) for more details concerning the implementation of the hash table.

The data representation provided herein would be quite efficient for dynamically changing graphs in the network randomization for two reasons. First, considering the scale-free properties of the high-resolution brain network, the degree distribution typically follows a power law, and most nodes have only a small number of connections (van den Heuvel, Stam, Boersma, & Hulshoff Pol, 2008; Wang et al., 2013). Second, the distribution of the nodal degree remains identical to the original network during the random rewiring process (Maslov & Sneppen, 2002). Therefore, the number of edges stored in the hash

table does not change, ensuring the memory efficiency of the proposed data representation.

## 2.4 | Module detection

In the PAGANI Toolkit, we implemented two module detection algorithms that are widely used in connectomics studies. These two partition methods can be applied for both binary and weighted networks. The algorithms detect modules that maximize the modularity measurement  $Q$  value in different ways. The first algorithm applies a spectral partition method (Newman, 2006), which was accelerated on GPUs in a previous study (Wang et al., 2013). In each round, a large module was divided into two submodules until no improvement in  $Q$  was found, and the best division for maximizing  $Q$  relied on the eigenvector that corresponded to the largest positive eigenvalue of the so-called modularity matrix. We accelerated the iterative power method for the computation of the eigenvector on GPUs. According to other graph analysis tools (e.g., BCT and GREYNA), a small modification was made to the original program to improve the modularity results. Specifically, the greedy method was performed to fine-tune the original eigenvector-based partition results at the end of each round. However, this process spends too much time on the iterative calculation of alterations in  $Q$  by moving each node in one submodule to the other. Again, we accelerated this iterative process on GPUs to an acceptable time for high-resolution networks with relatively sparse connectivity.

Another popular Louvain modularity algorithm implemented in the PAGANI Toolkit is based on an iterative heuristic partition method (Blondel et al., 2008). This algorithm includes two phases that repeat iteratively. The first phase attains the local maximum of the modularity by moving each node to the community for which the gain of modularity is maximum. The second phase builds a new network comprising hypernodes of the communities obtained in the first phase as the input network for the next iteration. The algorithm complexity is approximately linear on sparse networks because we only need to scan the neighbor communities of each node in the first iteration to calculate the maximum gain of modularity, and the number of communities dramatically declines after a few iterations. The module detection algorithms finally obtain the modularity  $Q$  value and a vector of community indices for each node in a network, which is required for the following computation of the participation coefficient (PC).

## 2.5 | Nodal metrics

The PAGANI Toolkit computes various nodal centrality metrics, including nodal degree, nodal efficiency, betweenness centrality (BC, only for binary networks), eigenvector centrality (EC) and PC (for detailed descriptions and definitions, see Supporting Information, Table S1). For a given node, its degree is defined as the number of edges in a binary network or the sum of the weights of the edges in a weighted network that directly connect to a node. Nodal BC measures the number of pairwise shortest paths that travel through a given node, which reflects its importance in the communication between other nodes. Nodal EC is defined as the first eigenvector corresponding to the principal

eigenvalue of an adjacent matrix and can capture an aspect of centrality that extends to global features of the graph (Bonacich, 1972; Zuo et al., 2012). Nodal PC describes the ratio between the intermodule and intramodule connections of a node, representing the ability to integrate the communication between different modules. Notably, nodes with high a PC are usually identified as “connector” hubs (He et al., 2009; Power, Schlaggar, Lessov-Schlaggar, & Petersen, 2013). The computations of nodal degree and PC take a short amount of time. Therefore, accelerating their computation is trivial.

In addition to these centrality metrics, the PAGANI Toolkit can also calculate nodal clustering coefficients (a measure of clustering in the neighborhood of a node) and nodal efficiency (a measure of the global efficiency of a node communicating with other nodes). These two metrics share the same computational programs with Cp and Lp, respectively, as mentioned in the previous section regarding global metrics. Here, we primarily focused on the acceleration of BC and EC computations.

BC is defined as the ratio of all shortest paths passing through a given node in the network, indicating the influence of a given node on information transfer through the network. BFS and a subsequent reverse traversal are two steps required for the computation of BC. We compared different accelerating strategies on the GPU (Pande & Bader, 2011; Sriram, Gautham, Kothapalli, Narayan, & Govindarajulu, 2009) and ultimately integrated parallel schemes from a study (Pande & Bader, 2011) into the PAGANI Toolkit according to experiments on commonly used 3- and 4-mm isotropic resolutions. In addition, a level synchronous BFS algorithm (Hong, Oguntebi, & Olukotun, 2011), which optimizes the pattern of GPU memory access, was used to compute BC.

EC is calculated using the power method. The basic operation of the power method is sparse matrix vector multiplication, which has been accelerated on GPU devices in several studies (Bell & Garland, 2008; Williams et al., 2009). For easy implementation and robustness, sparse matrix vector multiplication in the PAGANI Toolkit is performed by calling functions from the cuSPARSE library (<http://docs.nvidia.com/cuda/cusparse/index.html>). The cuSPARSE library was also employed in the spectral module detection to accelerate sparse matrix computations. The GPU-based library is composed of basic linear algebra subroutines utilized for sparse matrices and has better performance than the Intel MKL, a high-performance math library widely used in CPU programming (<https://software.intel.com/en-us/intel-mkl/>).

## 2.6 | Data format

The PAGANI Toolkit employs connectivity matrices in a compressed sparse row (CSR) format (Langr & Tvrdik, 2015), a standard storage format for sparse matrices in scientific computing, as the inputs for computations in the graph-theoretical analysis. Briefly, as illustrated in Figure 4, a graph or network is traditionally represented by indices of two end-points and the connective weight of every edge in the graph, referred to as the coordinate (COO) format. The CSR format represents a connectivity matrix by three vectors denoted **R**, **C**, and **V**. The non-zero entries (i.e., the connective weights) in the matrix are contiguously stored in vector **V**, along with their column indices in vector **C**. Vector

**R** maintains the offset pointing to the first element of each row in vector **V** or **C**. For a binary network, all the nonzero weights are one; thus, vector **V** can be omitted. Compared with adopting entire connectivity matrices as the basic data structure in most existing connectome toolboxes, using the CSR format is more efficient for representing brain networks because the high-resolution brain networks are usually sparse and vectors **V** and **C** can be very small. The theoretical space complexity for the storage of a network matrix decreased from  $O(n^2)$  to  $O(n + m)$ , where  $m$  is the number of links in a network.

After providing a working directory, the PAGANI Toolkit calculates the topological metrics ticked in the GUI panel for all networks (CSR format files) under the directory. Global metrics, including Cp, Lp, modularity, Gamma, Lambda, and Sigma, are exported as text files. Nodal metrics, including nodal efficiency, degree, nodal clustering coefficient, PC, BC, and EC, are automatically converted to 3D NIFTI files. For functional networks, the toolbox offers a GPU-based program to accelerate network construction from functional imaging data in common NIFTI files. A MATLAB function, which converts connectivity matrices into CSR format files, is also provided in the software package for compatibility with other connectomes from different modalities.

## 2.7 | Example R-fMRI data

### 2.7.1 | Data acquisition and preprocessing

We used a publicly available dataset from the HCP S900 release (Van Essen et al., 2012) to illustrate the application of the PAGANI Toolkit. This dataset contains R-fMRI data from 873 healthy young adults. Individual functional images include 1,200 frames of multiband, gradient-echo planar imaging data acquired during a period of 14 min and 33 s with the following parameters: TR = 720 ms; TE = 33.1 ms; FA = 52°; FOV = 280 × 180 mm<sup>2</sup>; matrix = 140 × 90 mm<sup>2</sup>; and 2-mm isotropic voxel size. During data acquisition, individuals fixated on a bright cross-hair projected on a dark background. Two phase-encoding directions (left-to-right and right-to-left) were used in each session during R-fMRI data acquisition. Here, we only used the left-to-right-encoded runs to avoid potential effects of different phase-encoding directions on our findings. The original R-fMRI data were minimally preprocessed (Glasser et al., 2013) with gradient distortion correction, head motion correction, image distortion correction, spatial normalization to the Montreal Neurological Institute (MNI) space, and intensity normalization.

We further reduced the biophysical and other noise in the minimally preprocessed data with DPARSF (Yan & Zang, 2010) and SPM8 (<http://www.fil.ion.ucl.ac.uk/spm>). Additional preprocessing procedure included linear detrending, nuisance signals regression (24 head motion parameters and cerebrospinal fluid, white matter, and global signals), and temporal bandpass filtering (0.01–0.1 Hz). The data of 227 subjects were excluded because of excessive head motion (translation > 3 mm, rotation > 3°, or a mean frame-wise displacement > 0.2 mm), 21 subjects were excluded due to arachnoid cysts, and one subject was excluded due to missing time points. Finally, the data of 624 subjects (352 females and 272 males) were included in the further analysis (age: 22~36, 44 males, IQ: 16.7 ± 4.9, ER: 35.5 ± 2.6). IQ stands for

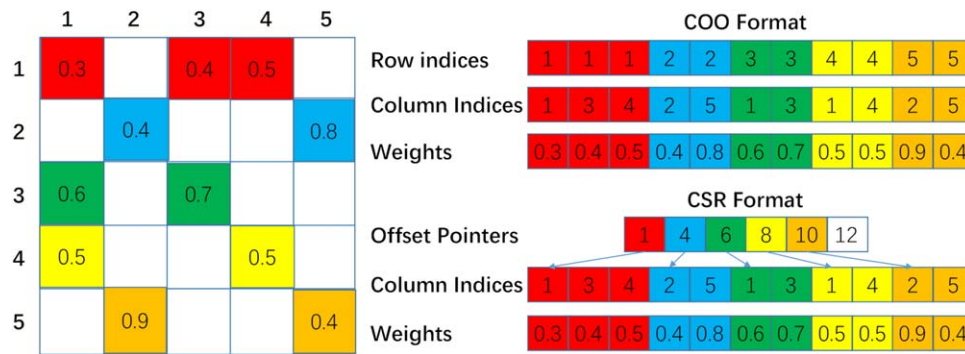


**FIGURE 4** A schematic of the coordinate (COO) format and compressed sparse row (CSR) format for the storage of a sparse connectivity matrix [Color figure can be viewed at [wileyonlinelibrary.com](http://wileyonlinelibrary.com)]

intelligence quotient. ER stands for emotion recognition score, which is the number of correct responses in the Penn Emotion Recognition Test. The distributions of IQ and ER are illustrated in Supporting Information, Figure S1.

### 2.7.2 | Functional network construction

A gray matter (GM) mask of 195,144 voxels was generated from a prior GM probability map (threshold at 0.2) provided by SPM8. We calculated Pearson's correlations between all pairs of nodes (i.e., GM voxels) and removed all negative correlations considering their vague biological interpretation (Murphy & Fox, 2017; Schwarz & McGonigle, 2011). Then, we constructed functional networks for each subject at a connectivity density threshold of 0.1%. The selected density ensures the sparse nature of the brain networks and simultaneously maintains estimable small-world properties. The PAGANI Toolkit accelerated both the computation of the correlation matrix and the subsequent thresholding procedure on GPUs for the functional network construction. The detailed optimization of functional network construction can be found in our previous work (Zhao, Du, & Wang, 2017).

### 2.7.3 | Network analysis

A variety of global (Cp, Lp, Gamma, Lambda, small-worldness, and modularity) and nodal (nodal degree, nodal efficiency, nodal BC, EC, and PC) topological metrics were calculated for the binary networks of 624 subjects. Here, we applied the spectral partition algorithm for module detection, and five surrogate random networks were generated for each network for the calculation of small-world properties. Spatial maps of nodal metrics were smoothed with an 8-mm isotropic FWHM Gaussian kernel using SPM8. We attained the group-level maps at each density by averaging the individual maps across subjects for all nodal metrics. These maps were further normalized to z-scores by subtracting the mean and dividing by the standard deviation. Functional hubs were identified based on the criterion of one standard deviation above the mean value of nodal centralities across the brain (i.e., z-score > 1).

### 2.7.4 | Statistical analysis

We performed the following statistical analysis at each network density. First, we investigated whether there were between-gender differences in the global and nodal network metrics using a general linear model (GLM) with the network metric as the dependent variable,

gender as the independent variable, and age as a covariate. Then, to determine whether the network metrics were related to individual cognitive abilities (i.e., IQ and ER) and whether these relationships were different in males and females, another GLM was used to elucidate the interactive and main effects of cognitive abilities and sex on each graph metric. The network metric again served as the dependent variable, with the cognitive score (i.e., IQ or ER), sex, and the product of the cognitive score and sex as the independent variables and age as a covariate. Notably, the statistical analysis for nodal metrics was performed in a voxel-wise fashion, and the significance level was set to  $p < 0.001$  at the voxel level with family-wise error (FWE) correction to  $p < 0.05$  for multiple comparisons at the cluster level.

### 2.7.5 | Validation analysis

To validate the robustness of the global architecture of the high-resolution functional brain networks, we examined the influence of different image preprocessing and data analysis strategies, including the use of different network densities (0.05%, 0.1%, and 0.15%) and pre-processed data without global signal regression. Due to the limited computation resources, we performed these validation analyses on a subdataset of 134 subjects from the HCP Q2 data release. After excluding 9 subjects with excessive head motion or missing time points, the data of 125 subjects were finally used in the analysis.

## 3 | RESULTS

The release version of the PAGANI Toolkit is published and can be downloaded freely from the NITRC website ([https://www.nitrc.org/projects/pagani\\_toolkit/](https://www.nitrc.org/projects/pagani_toolkit/)), and the source code is uploaded on GitHub for open-source development. The evaluation of the software performance was under a computing environment comprising an Intel (R) Core (TM) i7-3770 quad-core CPU @ 3.4 GHz with 64 GB RAM for CPU programs, the NVIDIA GeForce GTX TITAN Black (5.5 GB GPU memory) for GPU programs, and a 64-bit Windows operating system.

### 3.1 | The calculation performance of the PAGANI toolkit

To demonstrate the efficiency of the PAGANI Toolkit for mapping human connectomes under different resolutions, we conducted a

TABLE 2 The performance of the PAGANI Toolkit at different network scales

Network scale (resolution) Density		~60 K (3-mm)			~200 K (2-mm)		~1.6 M (1-mm) 0.01%
		0.10%	1.00%	10.00%	0.10%	1.00%	
Performance		Runtime/memory (min/GB)					
FNC (GPU)		0.1/0.52	0.1/0.8	0.1/3.3	1.0/1.5	1.0/4.3	59.4/9.8
Small-world properties	Cp (CPU)	0.2/0.1	0.6/0.3	6.5/1.3	1.4/0.2	45.3/1.5	8.2/1.1
	Lp (GPU & CPU)	1.4/0.1	8.1/14.3	8.1/15.5	58.5/0.2	514.1/1.4	-
	RNG (CPU)	0.1/0.1	0.35/3.6	3.0/4.6	0.7/0.9	7.3/6.0	4.4/6.4
Module detection	Louvain (CPU)	0.8/0.2	0.2/0.3	0.5/2.6	2.0/1.6	6.7/2.9	199.7/1.9
	Newman (GPU)	0.3/0.3	0.8/1.0	3.6/8.1	4.6/1.1	26.6/8.9	95.1/5.9
Nodal centralities	Deg. (CPU)	0.0/0.0	0.0/0.6	0.0/2.6	0.0/0.4	0.0/3.1	0.0/1.9
	PC (CPU)	0.0/0.0	0.0/0.6	0.0/2.6	0.0/0.4	0.0/3.1	0.0/1.9
	EC (GPU)	0.1/0.0	0.0/0.4	0.0/1.7	0.0/0.7	0.1/4.6	0.1/2.9
	BC (GPU)	3.2/0.1	59.2/0.2	~10 <sup>3</sup> /1.5	149.1/0.3	-	-

Note. Abbreviations: BC = betweenness centrality; Cp = clustering coefficient; EC = eigenvector centrality; FNC = functional network construction; Lp = characteristic path length; PC = participation coefficient; RNG = random network generation.

These results are for binary networks. For weighted networks, please refer to Supporting Information, Table S2. The nodal clustering coefficient and efficiency are not included because they share the same computational module with Cp and Lp.

The symbol “-” indicates that the computation cannot finish in 24 h.

comprehensive evaluation of its performance, including the elapsed time and memory usage, on a wide variety of network scales at different imaging resolutions. We resliced the original images of one randomly selected subject from 2-mm isotropic resolution (~200,000 voxels within the mask) to 1-mm and 3-mm isotropic resolutions (~1,600,000, and ~60,000 voxels, respectively).

Table 2 shows the performance of the computations for network metrics at several typical densities under different resolutions: 0.1%, 1%, and 10% densities for 3-mm resolution, 0.1% and 1% densities for 2-mm resolution, and 0.01% density for 1-mm resolution; most computations finished in an acceptable run time with tolerable memory usage. Specifically, for 3-mm resolution, the GPU-based network construction required only 0.1 min, independent of network density. For network densities of 0.1%–10%, most network computations were completed in a few minutes (e.g., Cp: 0.2–6.5 min; network randomization: 0.1–3.0 min; module detection: 0.2–0.8 min for the Louvain heuristic algorithm; and 0.3–3.6 min for the Newman spectral algorithm). For 2-mm resolution, the network construction required ~1 min. For network densities of 0.1%–1%, the computing time for most network metrics slightly increased (Cp: 1.4–45.3 min; network randomization: 0.7–7.3 min; module detection: 2.0–6.7 min for the Louvain algorithm; and 4.6–26.6 min for the Newman algorithm). For 1-mm resolution, the run time for network construction increased to ~1 h. Most computations were completed in an acceptable time at 0.01% density (Cp: 8.2 min; network randomization: 4.4 min; module detection: 199.7 min for the Louvain algorithm; and 95.1 min for the Newman algorithm). Among all network sizes and densities, PC and EC were computed in almost real time (<3 s). Computations of Lp and BC using the BFS algorithm had the highest complexity. The running time took only a few minutes at 0.1% density for 3-mm resolution but dramatically increased with growing network sizes and densities. Here, computation performances for the nodal clustering coefficient and nodal efficiency are not listed in the table because they were included in the calculation of Cp and Lp.

Notably, a GPU-based BFW algorithm was used to compute Lp at 1% and 10% densities under 3-mm resolution. The time cost of the BFW algorithm, primarily determined by the number of nodes, remained stable, costing ~8 min at these two densities. However, the BFW algorithm occupies ~15 GB memory for the storage of a distance matrix. The high space complexity limits its application in large network analyses at higher resolutions. Except for computing Lp using the BFW algorithm, the PAGANI Toolkit showed good memory efficiency for the computations of most metrics and used less than 10 GB of memory for all network sizes and densities in the experiments due to algorithm optimization based on a CSR format. In contrast, most of the existing graph-based toolboxes adopt an entire connectivity matrix that stores  $n^2$  entries to represent a network. An entire voxel-wise functional connectivity network theoretically requires approximately 15 GB, 140 GB, and 9 TB for 3-mm, 2-mm, and 1-mm isotropic resolutions, respectively, regardless of the edge density.

The computation time and memory usage largely rely on the network size and density; the acceptable density range decreases with increasing network size. Here, we provide a guideline for the approximate highest density thresholds for different network scales (Table 3). The thresholds are given under the constraints of either a reasonable time consumption (<200 min) or memory requirements available in the system (<45 GB).

Functional network construction, network randomization, heuristic module detection, and the computations of degree and PC are mainly restricted by memory constraints, with the highest acceptable density thresholds over 10% at 2-mm resolution and 0.1% at 1-mm resolution. The computations of BC, Cp, and Lp (together with the nodal clustering coefficient and nodal efficiency) are limited by computational speed and a lower density range that can be handled within the time limit. The computation of BC is the most time-consuming step, and the highest density reached 3%, 0.11%, and 0.0002% for 3, 2, and 1-mm isotropic resolution data, respectively. The GPU-based BFW algorithm

**TABLE 3** The maximum acceptable density threshold for different computations and network scales

Network scale (resolution)	Maximum acceptable density (%)							
	FNC	Cp/ci	Lp/ei	RNG	Newman/EC	Louvain	Deg/PC	BC
~60 K (3-mm)	~	25.0	~	~	13.0	~	~	3.0
~200 K (2-mm)	15.0	2.1	0.4	13.0	1.1	15.0	30.0	0.11
~1.6 M (1-mm)	0.2	0.1	0.004	0.1	0.017	0.2	0.4	0.0002
Limitation	mem.	time	time	mem.	GPU mem.	mem.	mem.	time

Note. Abbreviations: BC = betweenness centrality; Cp/ci = global and nodal clustering coefficient; EC = eigenvector centrality; FNC = functional network construction; Lp/ei = characteristic path length and nodal efficiency; RNG = random network generation; PC = participation coefficient.

The symbol “~” indicates that there is no theoretical density limit under the given time (<200 min) and memory (<45 GB) constraints and network scale.

can be used to calculate the Lp values for networks at an arbitrary density at 3-mm resolution, but it is not available at 2-mm or higher resolutions due to the memory limitation.

The GPU-based eigenvector method applied in the computation of EC and in Newman module detection is primarily limited by the capacity of GPU memory (5.5 GB) where the sparse network matrix is loaded (highest densities: 13% for 3-mm, 1.1% for 2-mm, and 0.017% for 1-mm isotropic resolutions). Notably, the execution time of both module detection methods also depends on the modular structure of a network, varying greatly among different subjects and network densities. For example, a lower network density could result in an increase in separated modules in a network, thus reducing the convergence speed of module detection.

Together, these results suggest that the PAGANI Toolkit shows high performance for analyzing high-resolution networks and offers a guideline for researchers to estimate computational time consumption and to choose a network scale with an appropriate density range when using the software toolbox.

### 3.2 | Parallel speedup compared to a single-core CPU toolkit

We first compared the parallel implementation in PAGANI to a typical single-core CPU version used by popular graph-based tools (e.g., GREYNA). The comparison was performed under three network scales ( $n = 5,353$ ,  $8,187$ , and  $11,044$ ) and network densities from 1% to 10%. Different network scales were generated from a GM probability map (4-mm isotropic resolution) with different thresholds (i.e., 0.6, 0.65, and 0.7). The parallel implementation in PAGANI showed extensive speedup for most of the computations (Supporting Information, Table S2). Specifically, the GPU-based BFW algorithm achieved the best speedup in the analysis ( $n = 5,353$ : 292.8- to 333.2-fold speedup;  $n = 8,187$ : 408.5- to 486.8-fold speedup;  $11,044$ : 551.3- to 568.2-fold speedup). Multicore acceleration for Cp achieved the least improvement in speed: a 7.7- to 16.7-fold increase among all conditions.

Next, we reimplemented a single-core version based on the CSR format to make it scalable to the 2-mm resolution HCP dataset; we compared the analysis time for one randomly selected subject with the parallelized computation components in PAGANI (Table 4).

Generally, GPU-based acceleration achieved an approximate a 350-fold increase in speed for the network construction, a 4.5- to 7.9-fold increase for modularity, a 2.9- to 11.8-fold increase for EC, and a 4.9- to 6.6-fold increase for betweenness. Notably, the computations of the correlation matrix can be more efficient using high-performance math libraries, such as the Intel MKL and the AMD ACML. These libraries can help achieve up to 10-fold increases in speed on the same multi-core CPU compared with that of the single-thread baseline in the comparison. Nevertheless, the GPU-based algorithm is still more efficient, achieving approximately a 30-fold increase in speed compared with that of these high-performance libraries. Multicore CPU acceleration using 8 threads led to a 4.6- to 5.1-fold speed increase for Cp and a 3.6- to 3.7-fold increase for Lp. Together, considering the computations for all three densities and the computations of Cp and Lp for the five-surrogate random network, the analysis in total spent ~27 h for one subject using the PAGANI Toolkit on a single machine. In contrast, the elapsed time would be 118 h running on the single-core CPU.

### 3.3 | The topological properties of high-resolution functional brain networks

#### 3.3.1 | Global metrics and hubs of high-resolution functional brain networks

The voxel-based functional networks of almost all the individuals exhibited stable small-world characteristics ( $\text{Sigma} = 3.51 \pm 1.56$ ). Meanwhile, the voxel-based functional networks also exhibited prominent modular architectures ( $Q = 0.61 \pm 0.06$ ) (Table 5).

The probability distribution of all nodal centrality fitted well with exponential truncated power law scaling, decaying as  $p(x) \sim a(x^b) \exp(-x/c)$  (Figure 5a). The global functional hubs identified based on nodal degree, BC, and EC exhibited similar spatial distribution patterns (the yellow regions with black boundaries in Figure 5b) and were primarily located in the default-mode network (DMN) [e.g., the bilateral precuneus (PCu), the medial prefrontal cortex (MPFC), and the inferior parietal lobule], the fronto-parietal network (FPN) [e.g., the dorsolateral prefrontal cortex and superior parietal cortex], the salience network [e.g., the dorsal anterior cingulate cortex (dACC)], and the primary visual cortex. The connector hubs with high PC values were mainly identified in the FPN [e.g., the dorsolateral prefrontal cortex and superior parietal cortex] (Figure 5b). A correlation analysis revealed that degree,

TABLE 4 Speedup of using the PAGANI Toolkit compared with a single-thread CPU platform

Computations		GPU				Multicore CPU	
		F. N. C.	Modularity	EC	BC	Cp	Lp
0.05% density	Baseline		734.8	4.4	$2.5 \times 10^4$	130.9	$7.2 \times 10^3$
	PAGANI		162.1	2.9	$3.8 \times 10^3$	26.5	$2.0 \times 10^3$
	Speedup		4.5	1.5	6.6	4.9	3.6
0.10% density	Baseline		$1.7 \times 10^3$	8.4	$5.4 \times 10^4$	385.7	$1.3 \times 10^4$
	PAGANI		277.3	1.0	$1.1 \times 10^4$	84.7	$3.5 \times 10^3$
	Speedup		6.2	8.3	4.9	4.6	3.7
0.15% density	Baseline	$2.1 \times 10^4$	$3.1 \times 10^3$	13.4	$7.5 \times 10^4$	727.6	$1.9 \times 10^4$
	PAGANI	60.1	390.4	1.1	$1.5 \times 10^4$	142.3	$5.2 \times 10^3$
	Speedup	350.0	7.9	11.8	5.0	5.1	3.7

Note. Abbreviations: BC = betweenness centrality; Cp = clustering coefficient; EC = eigenvector centrality; FNC = functional network construction; Lp = characteristic path length.

In the analysis of the example dataset, networks at 0.05% and 0.1% densities were generated from the network at 0.15% density without repeated computations of the correlation matrix during the network construction. Therefore, we only consider the runtime at 0.15% density for functional network construction.

BC, and EC had high spatial correlations between each other ( $r$  values  $> 0.84$ ) but relatively low correlations with PC ( $r$  values  $< 0.66$ ) (Supporting Information, Table S4).

### 3.3.2 | Between-gender differences in network topologies

Among the global metrics, we found that only modularity was significantly higher in the female group than that in the male group ( $T = 3.86$ ,  $p < 0.001$ , Bonferroni corrected, Supporting Information, Figure S2). The spatial distribution of all four nodal metrics (i.e., degree, BC, EC, and PC) was highly similar between the two gender groups (all  $r$  values  $> 0.8$ ,  $p$  values  $< 10^{-6}$ ). Nodal-level statistical analyses revealed that the male group, compared with the female, had significantly lower BC in a widespread bilateral regions over the medial/lateral frontoparietal and occipital cortices, including the precuneus/posterior cingulate cortex (PCu/PCC), superior frontal gyrus (SFG), insular cortex and thalamus. Males also had a significantly higher degree in the left cerebellum and inferior occipital gyrus but a lower degree in the bilateral PCu/PCC (Figure 6). No significant differences were observed between the two gender groups for EC and PC.

### 3.3.3 | Correlation between network metrics and cognitive behaviors

Neither significant interactive effects between IQ (or ER) and gender nor main effects of IQ (or ER) were observed for any of the global metrics. However, the nodal degree, BC, and EC showed significant negative correlations with IQ in several frontal regions: the left medial orbitofrontal cortex (OFCmed) for nodal degree; the left frontal gyrus for BC; and the bilateral olfactory cortex and the right middle frontal gyrus for EC. No significant interactive effect was found between cognitive abilities (IQ/ER) and gender on nodal metrics (Figure 7).

### 3.3.4 | Validation

The validation analysis for the HCP Q2 dataset revealed consistent small-world and modular architectures for individual voxel-wise functional networks at different densities with the main findings, with

Sigma ranging from 3.66 to 3.96 and modularity  $Q$  inversely related to the network density ranging from 0.6 to 0.67, respectively. Functional hubs showed similar spatial distribution patterns across different densities, with global hubs located in the regions of the DMN and the visual cortex, and connector hubs mostly located in the FPN.

Regarding global signal regression, we found that the voxel-based functional network derived from non-global signal-regressed data retained predominant small-world and modular architectures (Sigma =  $1.43 \pm 1.22$  and  $Q = 0.46 \pm 0.14$ ). However, compared to networks derived from global signal-regressed data, significantly lower Cp, Gamma, Sigma and  $Q$  and significantly higher Lp and Lambda were observed (all  $p$  values  $< 0.01$ , Bonferroni corrected). Moreover, we showed a significant negative correlation between BC and IQ in the left inferior/middle occipital gyrus (IOG/MOG) and the left opercular part of the inferior frontal gyrus. No significant differences were found between genders.

## 4 | DISCUSSION

We developed the PAGANI Toolkit based on a CPU-GPU hybrid framework (Wang et al., 2013) to automatically and rapidly compute the topological characteristics of high-resolution brain networks. The PAGANI Toolkit enhances the applicability and efficacy of high-resolution brain network analysis and facilitates "Big Data" research in human connectomics. This software provides a user-friendly GUI to customize computations with different parameter settings, such as the

TABLE 5 The quantitative values of global metrics

Measure	Cp	Gamma	Lp	Lambda	Sigma	Q
Mean	0.22	4.99	5.40	1.46	3.51	0.61
Std	0.05	2.13	2.25	0.25	1.56	0.06
Min	0.07	1.03	3.06	1.11	0.30	0.41
Max	0.32	16.49	21.42	3.57	12.58	0.75

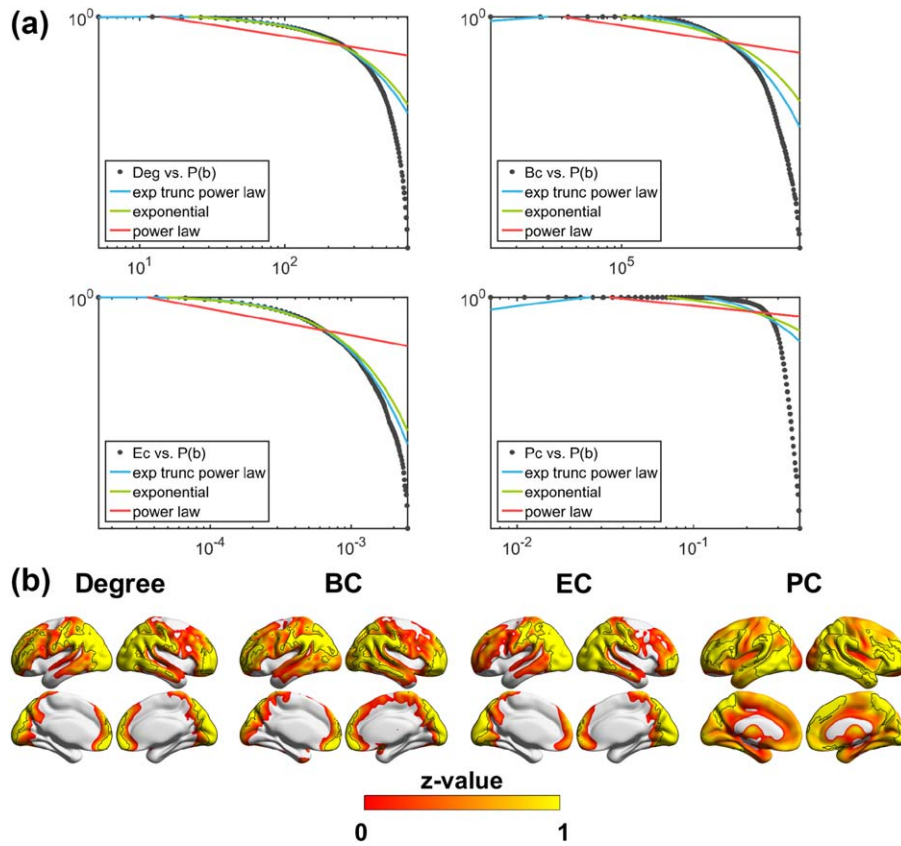


**FIGURE 5** The probability distribution and functional hubs identified by degree, EC, BC, and PC. (a) The probability distribution of nodal centralities fitted  $p(x) \sim a(x^b) \exp(-x/c)$  with estimated parameters:  $a = 0.86, b = 0.097, c = 133.6$  for degree;  $a = 0.04, b = 0.33, c = 2.2 \times 10^5$  for BC;  $a = 2.58, b = 0.082, c = 3.3 \times 10^{-4}$  for EC;  $a = 8.23, b = 0.52, c = 0.12$  for PC. (b) For each metric, regions with z-scores greater than 1 were defined as hubs, indicated by the yellow color. EC, eigenvector centrality; BC, betweenness centrality; PC, participation coefficient [Color figure can be viewed at [wileyonlinelibrary.com](http://wileyonlinelibrary.com)]

network type and thresholding strategy. The computation components are packaged into independent executable files with necessary libraries and are simple to set up without complicated configuration of the

computing environment. Moreover, we utilized a publicly available R-fMRI dataset under 2 mm isotropic resolution to demonstrate the capabilities of the PAGANI Toolkit.

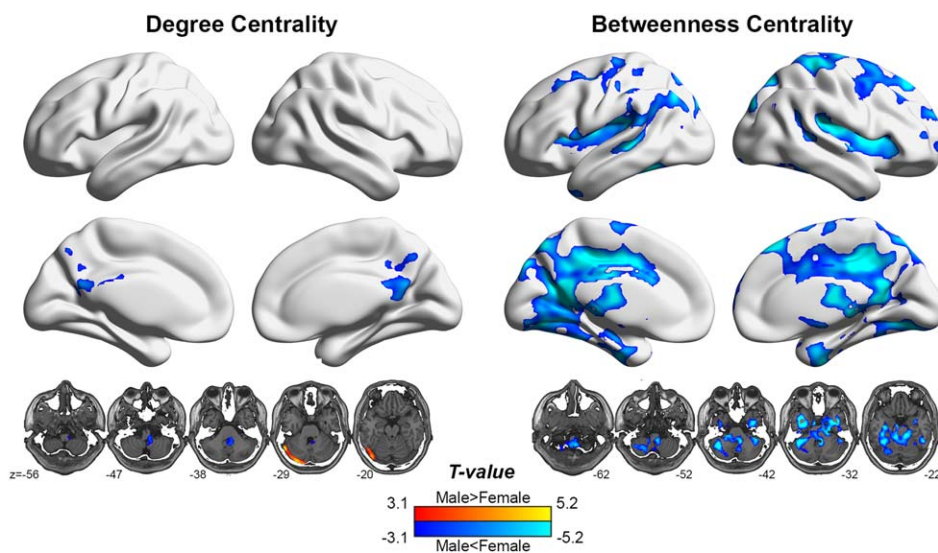


**FIGURE 6** Between-gender differences for the nodal degree and betweenness centrality. The significance level was set to  $p < .001$  at the voxel level with family-wise error (FWE) correction to  $p < .05$  for multiple comparisons at the cluster level. The image of the surface mapping was obtained using BrainNet Viewer (Xia, Wang, & He, 2013) [Color figure can be viewed at [wileyonlinelibrary.com](http://wileyonlinelibrary.com)]

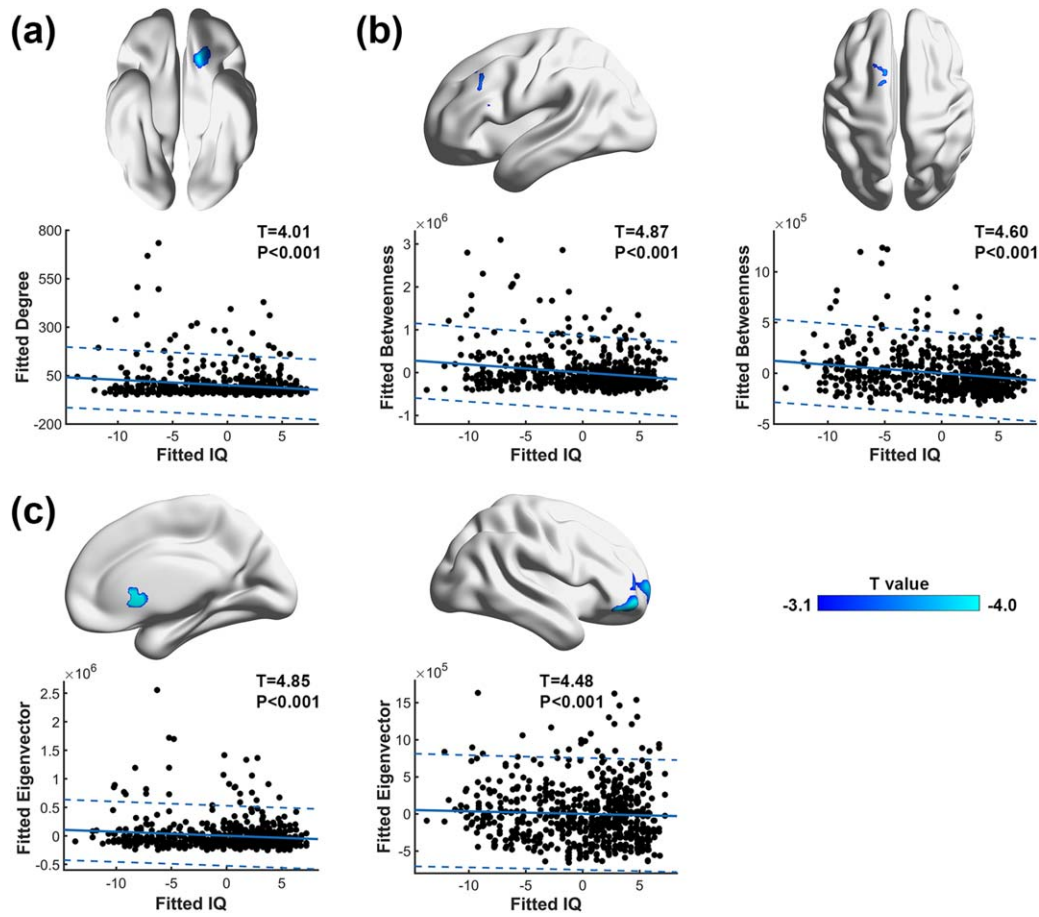


**FIGURE 7** Significant correlation between IQ and voxel-wise nodal degree (a), betweenness (b), and eigenvector centrality (c) in the T-value maps. The scatterplots illustrate the main effects of IQ on nodal metrics from the GLM analyses at the voxel of the peak T-value in (a) the left medial orbitofrontal cortex for degree, (b) the left frontal gyrus for betweenness, and (c) the olfactory cortex and middle frontal gyrus for eigenvector centrality. The significance level was set to  $p < .001$  at the voxel level with family-wise error (FWE) correction to  $p < .05$  for multiple comparisons at the cluster level. The diagram shows the fitted IQ and degree/BC because the age effect has been regressed as a covariate [Color figure can be viewed at [wileyonlinelibrary.com](http://wileyonlinelibrary.com)]

#### 4.1 | Advantages of the PAGANI toolkit

Compared with various existing graph-based tools, for example, BCT (Rubinov & Sporns, 2010) and GREYNA (Wang et al., 2015), the PAGANI Toolkit optimized the performance and scalability of graph-based approaches for large connectomes with thousands to millions of voxels from different modalities and species. Reflecting the high computation complexity and lack of efficient computational tools, most studies currently use a compromised ROI-based method or downsample the imaging data at a coarse level, potentially leading to loss of some important connectivity information. For example, Zuo et al. (2012) and Du et al. (2015) downsampled high-resolution imaging datasets to a 4-mm resolution when computing graph metrics at a voxel-wise level. Liao et al. (2013) utilized 3-mm isotropic resolution datasets in a study of the test-retest reliability of functional hubs. Tomasi, Shokri-Kojori, and Volkow (2016) utilized HCP datasets under the original 2-mm resolution for functional network analyses and suggested optimal parameters for the network threshold, the filtering bandwidth range, and the global signal normalization to increase the reliability of

the local functional connectivity density. However, these studies only calculated the nodal degree or strength of connectivity with neighboring regions to identify the local functional connectivity density. To our knowledge, there are no reports on either the global or nodal topological characteristics of voxel-wise functional brain networks from datasets at 2 mm (or higher) resolution, although such resolutions have increasingly become more common in data collection. Thus, the developed PAGANI Toolkit provides the possibility to facilitate the study of human connectomes derived from currently available noninvasive imaging big data at their original resolution.

The computation components of the PAGANI Toolkit are based on a hybrid CPU-GPU platform proposed in a previous study (Wang et al., 2013). Compared with the previous platform, several improvements have been made to the current software toolbox. First, we integrated more functionalities in the platform, including analysis of the weighted network, a module detection program based on a heuristic algorithm (Blondel et al., 2008), and new computation components for BC, EC, and PC. Second, we optimized the memory efficiency to make the toolbox scalable to extend network sizes with increasing resolutions. For

example, this software adopts a CSR format instead of an entire connectivity matrix as the data structure, which largely reduces the memory usage for computations of naturally sparse brain networks. Because the ordered structure of CSR is not suitable to represent a dynamic changing graph in the network randomization, we proposed a novel data representation combining a bitmap and a hash table to solve this problem. Third, for functional network construction, in addition to the GPU-based computation of the correlation matrix in the previous platform, we also implemented a subsequent thresholding process on GPUs. The entire procedure achieved up to a 350-fold increase in speed compared with that of single-thread CPU implementations. Finally, we improved the flexibility and usability by packaging all computation components with the necessary libraries and providing a GUI. Researchers can download and use the released software via the GUI without the complicated configuration of computing environment.

#### 4.2 | Computational limit of the PAGANI toolkit

The performance and scalability of the PAGANI Toolkit are optimized based on the sparse nature of voxel-wise brain networks. For a typical single-core implementation by existing graph-based tools, the memory requirements increase with the square quantity of nodes. However, the PAGANI Toolkit utilizes a CSR network representation, the memory requirements of which scale linearly with network size and density. In addition, the speed of most graph-based algorithms is related to network density. For example, the time complexity for computing BC and Lp (BFS) is  $O(nm)$ ,  $O(nk^2)$  for Cp, and  $O(m)$  for a single loop of heuristic and spectral module detection, where  $n$  is the number of nodes,  $m$  is the number of edges, and  $k$  is the average connection degree of a node. Although parallel acceleration in PAGANI can achieve tens to hundreds of speedup for some complex computations by traversing multiple nodes or edges concurrently, the elapsed time and memory usage still increase with the network density at a given network scale.

Network density is a major bottleneck for large voxel-wise brain network analysis because of its associated memory requirements and its impact on computation speed—the acceptable range of network density decreases with the increasing network sizes due to the improving imaging resolution. For a better understanding of the density limits, Table 3 provides a guideline for the approximate highest acceptable density thresholds for different resolutions.

#### 4.3 | Comparison with a distributed system

The development of a distributed system on large-scale clusters is a potential solution to the excessive computation required. For example, Boubela, Kalcher, Huf, Nasel, and Moser (2015) proposed a scalable technology for network construction and for the analysis of large fMRI data (2-mm isotropic resolution) with the application of an Apache Spark framework containing the GraphX library (Gonzalez et al., 2014) as a representative distributed solution to achieve large graph computing. The principal advantage of distributed systems is that they are essentially scalable to any arbitrarily large graph. However, the setup and maintenance of the cluster environment for a distributed system

are complicated and not friendly to most neuroimaging researchers. Moreover, the performance of a distributed system is largely affected by the imbalance of computational capability and the actual workload of different single computing nodes. For large graph computing, the frequent communication between these nodes also decreases the performance of the cluster. Indeed, recent single-machine systems are able to manage huge graphs with billions of connections and achieve a comparable performance to distributed systems (Chi et al., 2016; Kyrölä, Blelloch, & Guestrin, 2012). However, individual computing nodes in high-performance clusters typically have both CPUs and GPUs that provide promising computing power. The attempt to fully utilize the potential computing power of an individual node is also meaningful in distributed systems. The best computational model for “Big Data” research in human connectomics would be the combination of optimized single-machine and distributed systems. A single computing node completes the internal fine-grain parallelism within an individual network or subnetwork, and the distributed system realizes the high-level parallelism with low coupling degree between different networks or subnetworks.

#### 4.4 | Distinctions between voxel-based and atlas-based brain networks

The acquisition of high-resolution neuroimaging data can provide abundant connectomics information at a fine granularity. Compared with atlas- or ROI-based brain networks, analyses of voxel-wise brain networks allow full exploitation of high-resolution imaging data, with more naturally defined nodes without a prior parcellation atlas that drastically reduces the data resolution. Moreover, voxel-wise brain network analyses can reveal more detailed connectivity information, particularly for regions that contain multiple subdivisions, for example, the hippocampus and amygdala (Amunts et al., 2005), the lateral parietal cortex (Nelson et al., 2010), and the medial parietal cortex (Margulies et al., 2009). In contrast, a network defined based on a coarse-grained atlas usually considers the functional activity within a given ROI as homogeneous, ignoring the possible spatial inhomogeneity within large ROIs (Jiang et al., 2015). In addition, greater connectedness can be achieved with increasing network sizes, particularly at low connectivity densities (Fornito, Zalesky, & Bullmore, 2010).

In this study, the analysis results show that a high-resolution brain network retains remarkable small-world characteristics at low densities. The Sigma values (mean: 3.51) of the voxel-wise networks are slightly larger than the typical Sigma values ( $\sim 2.0$ ) of atlas-based networks reported in previous studies (Achard, Salvador, Whitcher, Suckling, & Bullmore, 2006; Salvador et al., 2005). Hayasaka and Laurienti (2010) reported higher Sigma and Gamma values in voxel-wise networks compared with ROI-based networks. Furthermore, studies also showed that group-level voxel-wise networks could have more prominent small-world properties, for example, Sigma = 111 (31,503 nodes, 0.043% density) (Eguiluz, Chialvo, Cecchi, Baliki, & Apkarian, 2005), and Sigma = 111.4 (58,523 nodes, 0.023% density) (Wang et al., 2013). Large Sigma values with low wiring costs may reflect cost-effectiveness and efficiency of voxel-wise brain network organization.

The voxel-wise maps of functional hubs in Figure 5 show that high-degree hubs were mainly located in some DMN regions such as the PCu and MPFC. Although similar results were found in atlas-based networks (Achard et al., 2006; Wang et al., 2011), the voxel-wise maps allowed precise localization of these hub regions and delineation of their boundaries without making a priori assumptions using anatomical constraints.

Notably, connectivity densities play an important role in determining the network topologies of the voxel-wise networks. Increasing network sizes typically lead to a decreasing network density range in practical analyses, which can affect the nature and interpretation of the resulting networks. Indeed, decreasing network density could lead to fewer long-range connections, which is more important for the global integration and communication of the whole network. As a result, the network may tend to have an increased  $L_p$  and a reduced small-world value but increased modular configurations (Du et al., 2015). In contrast, increasing network density would definitely favor the estimation of network efficiency but at a higher cost, which may have different implications for the cost-efficiency organization principle of the human brain network (Bullmore & Sporns, 2012). Therefore, in voxel-wise network analysis, sparse densities were commonly utilized for three main reasons. First, biologically, the human brain is optimally organized to a balance efficiency and cost. Second, mathematically, many graph theoretical metrics were less meaningful when the network connectivity became denser. Third, the computation resource was limited.

#### 4.5 | Characteristics of functional brain networks

Using a publicly available dataset from the HCP, we identified a stable small-world property in voxel-based functional networks and highly connected hubs located in the DMN, the salience network, the FPN, and the primary visual cortex. These results are consistent with those of previous voxel-based functional network studies (Du et al., 2015; Liao et al., 2013; van den Heuvel & Sporns, 2013). Significantly higher modularity and BC were observed in the female group mainly in the medial/lateral fronto-parietal and occipital cortices. Moreover, negative correlations were identified between IQ and node-level metrics (degree, BC, and EC) in several frontal regions.

Several previous studies have revealed gender-related differences in functional connectivity and brain networks (Gong, He, & Evans, 2011; Kilpatrick, Zald, Pardo, & Cahill, 2006; Tomasi & Volkow, 2012; Wu et al., 2013). For example, Tomasi and Volkow (2012) revealed gender-related differences in local functional connectivity density in many cortical and subcortical brain regions using a thresholding-by-correlation procedure, which is different from our study. Another ROI-based study revealed asymmetric differences in the clustering coefficients in the in two hemispheres between males and females (Tian, Wang, Yan, & He, 2011). These results may reflect distinct infrastructures of brain organization leading to cognitive and behavioral between-gender differences. In the present study, we found that the BC in the female group was higher in widespread bilateral regions across the medial/lateral fronto-parietal and occipital cortices, which may reflect the between-gender differences in some cognitive

functionalities correlated with these regions. For example, the PCu/PCC has been regarded as a network hub (van den Heuvel & Sporns, 2013) in the human brain associated with multiple cognitive functions including self-consciousness and memory (Fretton et al., 2014). The gender effects on nodal degree were twofold: the males possessed a higher degree in the left cerebellum and IOG, but a lower degree in the PCu/PCC. The cerebellum is involved in the regulation of various functional traits such as affection, emotion, and behavior (Turner et al., 2007). The IOG is related to visual functions such as face processing (Uono et al., 2017). Together, our findings in high-resolution functional networks provide further evidence of gender-related differences in behavioral and brain functions.

Using large-sample data (624 subjects), the present study found negative correlations between IQ and nodal centralities in different frontal regions. These regions are related to various cognitive functions. For example the left OFCmed is involved in the cognitive processing of decision-making (Kringelbach, 2005); the left SFG is related to self-awareness (Goldberg, Harel, & Malach, 2006); and the MFG (Brodmann area 25) participates in the regulation of emotion through the amygdala (Motzkin, Philippi, Wolf, Baskaya, & Koenigs, 2015) and is associated with memory and decision-making (Hebscher, Barkan-Abramski, Goldsmith, Aharon-Peretz, & Gilboa, 2016). Recent studies have demonstrated a significant association between the functional architectures of the human brain and cognitive abilities. For example, Finn et al. (2015) demonstrated that functional connectivity patterns are individualized and can be used to predict levels of individual intelligence. Hilger, Ekman, Fiebach, and Basten (2016) reported significant associations between the nodal efficiency in the dACC, the anterior insula, and the left temporo-parietal junction of the voxel-wise functional brain network and individual intelligence. They also observed a marginally significant correlation between IQ and global efficiency. Our results along with these findings provide empirical evidence illustrating the functional architectures that underlie human cognition and behavior.

#### 4.6 | Future studies

In the future, the PAGANI Toolkit will be improved in several ways. First, a future version of this toolbox will provide functionalities for network mapping of structural connectomes from diffusion MRI. For example, probabilistic fiber tractography methods (Behrens, Berg, Jbabdi, Rushworth, & Woolrich, 2007) have advantages for identifying multiple fiber orientations in diffusion tensor images but are extremely time-consuming. GPU-based algorithms would largely accelerate the process (Hernandez et al., 2013; Xu et al., 2012) and will be integrated into the toolbox in the future. Second, the computing performance for several high-complexity metrics, such as  $L_p$  and BC, is not satisfactory for large networks. To further improve the software platform, we intend to introduce state-of-the-art graph computing libraries, for example, NXgraph (Chi et al., 2016), a disk-based single-machine system, and CuSha (Khorasani, Vora, Gupta, & Bhuyan, 2014), a GPU-based graph computing framework. Furthermore, we will extend the toolbox to a cluster with multiple CPUs and GPUs to exploit the inter-subject parallelism for Big Data research using large datasets. As an

open-source project, we expect that the PAGANI Toolkit will promote the interest of outstanding computer scientists to contribute to studies of human connectomics and bridge the gap between the shortages of efficient computing modals and the rapidly growing computational requirements. Finally, we observed a significant effect of global signal regression on the calculation of network metrics, although both kinds of networks retained predominant small-world and modular architectures. fMRI studies have revealed that functional metrics could be affected by global signal regression for reduced BOLD spectral power and improvement in the detection of system-level correlations in resting-state brain networks (Du et al., 2015; Fox, Zhang, Snyder, & Raichle, 2009; Liang et al., 2012; Liu, Nalci, & Falahepour, 2017). However, the biological mechanism for the global signal remains largely unknown (Murphy & Fox, 2017; Qing, Dong, Li, Zang, & Liu, 2015; Saad et al., 2012; Schwarz & McGonigle, 2011). Future studies with combined imaging techniques and elegant experimental designs could provide critical information for a valuable neurobiological explanation of the global signal.

## ACKNOWLEDGMENT

This work was supported by the Natural Science Foundation of China (Grant Nos. 81401479, 81671767, 81620108016, 31521063, 61622403, and 61621091), the Beijing Natural Science Foundation (Grant Nos. Z161100004916027, Z151100003915082, Z161100000216152, and Z161100000216125), the Fundamental Research Funds for the Central Universities (Grant Nos. 2015KJCA13 and 2017XTCX04), and Changjiang Scholar Professorship Award (Award No. T2015027). Data were provided by the Human Connectome Project, WU-Minn Consortium (Principal Investigators: David Van Essen and Kamil Ugurbil; 1U54MH091657) funded by the 16 NIH Institutes and Centers that support the NIH Blueprint for Neuroscience Research; and by the McDonnell Center for Systems Neuroscience at Washington University. The authors declare no competing interests. We gratefully acknowledge the support of NVIDIA Corporation with the donation of the Tesla K40 GPU used for this research.

## ORCID

Mingrui Xia  <http://orcid.org/0000-0003-4615-9132>

Yong He  <http://orcid.org/0000-0002-7039-2850>

## REFERENCES

- Achard, S., Salvador, R., Whitcher, B., Suckling, J., & Bullmore, E. (2006). A resilient, low-frequency, small-world human brain functional network with highly connected association cortical hubs. *Journal of Neuroscience*, 26, 63–72.
- Amunts, K., Kedo, O., Kindler, M., Pieperhoff, P., Mohlberg, H., Shah, N. J., ... Zilles, K. (2005). Cytoarchitectonic mapping of the human amygdala, hippocampal region and entorhinal cortex: Intersubject variability and probability maps. *Anatomy and Embryology*, 210, 343–352.
- Barrat, A., Barthelemy, M., Pastor-Satorras, R., & Vespignani, A. (2004). The architecture of complex weighted networks. *Proceedings of the National Academy of Sciences of the United States of America*, 101, 3747–3752.
- Behrens, T. E., Berg, H. J., Jbabdi, S., Rushworth, M. F., & Woolrich, M. W. (2007). Probabilistic diffusion tractography with multiple fibre orientations: What can we gain? *NeuroImage*, 34, 144–155.
- Bell, N., & Garland, M. (2008). *Efficient sparse matrix-vector multiplication on CUDA*. Nvidia technical report NVR-2008-004. Nvidia Corporation.
- Blondel, V. D., Guillaume, J. L., Lambiotte, R., & Lefebvre, E. (2008). Fast unfolding of communities in large networks. *Journal of Statistical Mechanics: Theory and Experiment*, 2008, P10008.
- Bonacich, P. (1972). Factoring and weighting approaches to status scores and clique identification. *Journal of Mathematical Sociology*, 2, 113–120.
- Boubela, R. N., Kalcher, K., Huf, W., Nasel, C., & Moser, E. (2015). Big data approaches for the analysis of large-scale fMRI data using apache spark and GPU processing: A demonstration on resting-state fMRI data from the Human Connectome project. *Frontiers in Neuroscience*, 9, 492.
- Bullmore, E., & Sporns, O. (2012). The economy of brain network organization. *Nature Reviews Neuroscience*, 13, 336–349.
- Cao, M., He, Y., Dai, Z., Liao, X., Jeon, T., Ouyang, M., ... Huang, H. (2017). Early development of functional network segregation revealed by connectomic analysis of the preterm human brain. *Cerebral Cortex*, 27, 1949–1963.
- Cao, M., Huang, H., & He, Y. (2017). Developmental Connectomics from Infancy through Early Childhood. *Trends Neurosci*, 40, 494–506.
- Castellanos, F. X., Di Martino, A., Craddock, R. C., Mehta, A. D., & Milham, M. P. (2013). Clinical applications of the functional connectome. *NeuroImage*, 80, 527–540.
- Chi, Y., Dai, G., Wang, Y., Sun, G., Li, G., & Yang, H. (2016). NXgraph: an efficient graph processing system on a single machine. In: IEEE. p 409–420.
- Cohen, A. L., Fair, D. A., Dosenbach, N. U., Miezin, F. M., Dierker, D., Van Essen, D. C., ... Petersen, S. E. (2008). Defining functional areas in individual human brains using resting functional connectivity MRI. *NeuroImage*, 41, 45–57.
- Du, H. X., Liao, X. H., Lin, Q. X., Li, G. S., Chi, Y. Z., Liu, X., ... Xia, M. R. (2015). Test-retest reliability of graph metrics in high-resolution functional connectomics: A resting-state functional MRI study. *CNS Neuroscience & Therapeutics*, 21, 802–816.
- Eguiluz, V. M., Chialvo, D. R., Cecchi, G. A., Baliki, M., & Apkarian, A. V. (2005). Scale-free brain functional networks. *Physical Review Letters*, 94, 018102.
- Eklund, A., Dufort, P., Forsberg, D., & LaConte, S. M. (2013). Medical image processing on the GPU - past, present and future. *Medical Image Analysis*, 17, 1073–1094.
- Fan, L., Li, H., Zhuo, J., Zhang, Y., Wang, J., Chen, L., ... Jiang, T. (2016). The Human Brainnetome Atlas: A new brain atlas based on connective architecture. *Cerebral Cortex*, 26, 3508–3526.
- Ferreira, L. K., Regina, A. C., Kovacevic, N., Martin Mda, G., Santos, P. P., Carneiro Cde, G., ... Busatto, G. F. (2016). Aging effects on whole-brain functional connectivity in adults free of cognitive and psychiatric disorders. *Cerebral Cortex*, 26, 3851–3865.
- Finn, E. S., Shen, X., Scheinost, D., Rosenberg, M. D., Huang, J., Chun, M. M., ... Constable, R. T. (2015). Functional connectome fingerprinting: Identifying individuals using patterns of brain connectivity. *Nature Neuroscience*, 18, 1664–1671.
- Fornito, A., Zalesky, A., & Breakspear, M. (2015). The connectomics of brain disorders. *Nature Reviews Neuroscience*, 16, 159–172.
- Fornito, A., Zalesky, A., & Bullmore, E. T. (2010). Network scaling effects in graph analytic studies of human resting-state FMRI data. *Frontiers in Systems Neuroscience*, 4, 22.

- Fox, M. D., Zhang, D., Snyder, A. Z., & Raichle, M. E. (2009). The global signal and observed anticorrelated resting state brain networks. *Journal of Neurophysiology*, *101*, 3270–3283.
- Freton, M., Lemogne, C., Bergouignan, L., Delaveau, P., Lehericy, S., & Fossati, P. (2014). The eye of the self: Precuneus volume and visual perspective during autobiographical memory retrieval. *Brain Structure and Function*, *219*, 959–968.
- Glasser, M. F., Coalson, T. S., Robinson, E. C., Hacker, C. D., Harwell, J., Yacoub, E., ... Van Essen, D. C. (2016). A multi-modal parcellation of human cerebral cortex. *Nature*, *536*, 171–178.
- Glasser, M. F., Sotiropoulos, S. N., Wilson, J. A., Coalson, T. S., Fischl, B., Andersson, J. L., ... Jenkinson, M. (2013). The minimal preprocessing pipelines for the Human Connectome Project. *NeuroImage*, *80*, 105–124.
- Goldberg, I. I., Harel, M., & Malach, R. (2006). When the brain loses its self: Prefrontal inactivation during sensorimotor processing. *Neuron*, *50*, 329–339.
- Gong, G., He, Y., & Evans, A. C. (2011). Brain connectivity gender makes a difference. *The Neuroscientist*, *17*, 575–591.
- Gonzalez, J. E., Xin, R. S., Dave, A., Crankshaw, D., Franklin, M. J., & Stolica, I. (2014). GraphX: Graph processing in a distributed dataflow framework. pp. 599–613.
- Grayson, D. S., & Fair, D. A. (2017). Development of large-scale functional networks from birth to adulthood: A guide to neuroimaging literature. *NeuroImage* *160*, 15–31.
- Hayasaka, S., & Laurienti, P. J. (2010). Comparison of characteristics between region- and voxel-based network analyses in resting-state fMRI data. *NeuroImage*, *50*, 499–508.
- He, B., Dai, Y., Astolfi, L., Babiloni, F., Yuan, H., & Yang, L. (2011). eConnectome: A MATLAB toolbox for mapping and imaging of brain functional connectivity. *Journal of Neuroscience Methods*, *195*, 261–269.
- He, Y., Wang, J., Wang, L., Chen, Z. J., Yan, C., Yang, H., ... Evans, A. C. (2009). Uncovering intrinsic modular organization of spontaneous brain activity in humans. *PLoS One*, *4*, e5226.
- Hebscher, M., Barkan-Abramski, M., Goldsmith, M., Aharon-Peretz, J., & Gilboa, A. (2016). Memory, decision-making, and the ventromedial prefrontal cortex (vmPFC): The roles of subcallosal and posterior orbitofrontal cortices in monitoring and control processes. *Cerebral Cortex*, *26*, 4590–4601.
- Hernandez, M., Guerrero, G. D., Cecilia, J. M., Garcia, J. M., Inuggi, A., Jbabdi, S., ... Sotiropoulos, S. N. (2013). Accelerating fibre orientation estimation from diffusion weighted magnetic resonance imaging using GPUs. *PLoS One*, *8*, e61892.
- Hilger, K., Ekman, M., Fiebach, C. J., & Basten, U. (2016). Efficient hubs in the intelligent brain: Nodal efficiency of hub regions in the salience network is associated with general intelligence. *Intelligence*, *60*, 10–25.
- Hong, S., Oguntebi, T., & Olukotun, K. (2011). Efficient parallel graph exploration on multi-core CPU and GPU. In: IEEE. pp. 78–88.
- Hosseini, S. M., Hoefl, F., & Kesler, S. R. (2012). GAT: A graph-theoretical analysis toolbox for analyzing between-group differences in large-scale structural and functional brain networks. *Plos One*, *7*, e40709.
- Jiang, L., Xu, T., He, Y., Hou, X. H., Wang, J., Cao, X. Y., ... Zuo, X. N. (2015). Toward neurobiological characterization of functional homogeneity in the human cortex: Regional variation, morphological association and functional covariance network organization. *Brain Structure and Function*, *220*, 2485–2507.
- Keunen, K., Counsell, S. J., & Benders, M. J. (2017). The emergence of functional architecture during early brain development. *NeuroImage*, *160*, 2–14.
- Khorasani, F., Vora, K., Gupta, R., & Bhuyan, L. N. (2014). CuSha: Vertex-centric graph processing on GPUs. In: ACM. pp. 239–252.
- Kilpatrick, L. A., Zald, D. H., Pardo, J. V., & Cahill, L. F. (2006). Sex-related differences in amygdala functional connectivity during resting conditions. *NeuroImage*, *30*, 452–461.
- Kringelbach, M. L. (2005). The human orbitofrontal cortex: Linking reward to hedonic experience. *Nature Reviews Neuroscience*, *6*, 691–702.
- Kruschwitz, J. D., List, D., Waller, L., Rubinov, M., & Walter, H. (2015). GraphVar: A user-friendly toolbox for comprehensive graph analyses of functional brain connectivity. *Journal of Neuroscience Methods*, *245*, 107–115.
- Kyrola, A., Belloch, G. E., & Guestrin, C. (2012). GraphChi: Large-scale graph computation on just a PC. pp. 31–46.
- Langr, D., & Tvrđik, P. (2015). Evaluation criteria for sparse matrix storage formats. *IEEE Transactions on Parallel and Distributed Systems*, *27*, 428–440.
- Liang, X., Wang, J., Yan, C., Shu, N., Xu, K., Gong, G., & He, Y. (2012). Effects of different correlation metrics and preprocessing factors on small-world brain functional networks: A resting-state functional MRI study. *PLoS One*, *7*, e32766.
- Liao, X., Vasilakos, A. V., & He, Y. (2017). Small-world human brain networks: Perspectives and challenges *Neurosci Biobehav Rev*, *77*, 286–300.
- Liao, X. H., Xia, M. R., Xu, T., Dai, Z. J., Cao, X. Y., Niu, H. J., ... He, Y. (2013). Functional brain hubs and their test-retest reliability: A multi-band resting-state functional MRI study. *NeuroImage*, *83*, 969–982.
- Liu, T. T., Nalci, A., & Falahpour, M. (2017). The global signal in fMRI: Nuisance or Information? *NeuroImage*, *150*, 213–229.
- Margulies, D. S., Vincent, J. L., Kelly, C., Lohmann, G., Uddin, L. Q., Biswal, B. B., ... Petrides, M. (2009). Precuneus shares intrinsic functional architecture in humans and monkeys. *Proceedings of the National Academy of Sciences of the United States of America*, *106*, 20069–20074.
- Maslov, S., & Sneppen, K. (2002). Specificity and stability in topology of protein networks. *Science (New York, N.Y.)*, *296*, 910–913.
- Motzkin, J. C., Philippi, C. L., Wolf, R. C., Baskaya, M. K., & Koenigs, M. (2015). Ventromedial prefrontal cortex is critical for the regulation of amygdala activity in humans. *Biological Psychiatry*, *77*, 276–284.
- Murphy, K., & Fox, M. D. (2017). Towards a consensus regarding global signal regression for resting state functional connectivity MRI. *NeuroImage*, *154*, 169–173.
- Nelson, S. M., Cohen, A. L., Power, J. D., Wig, G. S., Miezin, F. M., Wheeler, M. E., ... Petersen, S. E. (2010). A parcellation scheme for human left lateral parietal cortex. *Neuron*, *67*, 156–170.
- Newman, M. E. (2006). Finding community structure in networks using the eigenvectors of matrices. *Physical Review E*, *74*, 036104.
- Newman, M. E. J. (2003). The structure and function of complex networks. *Siam Review*, *45*, 167–256.
- Onnela, J. P., Saramaki, J., Kertesz, J., & Kaski, K. (2005). Intensity and coherence of motifs in weighted complex networks. *Physical Review E, Statistical, Nonlinear, and Soft Matter Physics*, *71*, 065103.
- Pande, P., & Bader, D. A. (2011). Computing betweenness centrality for small world networks on a GPU.
- Power, J. D., Cohen, A. L., Nelson, S. M., Wig, G. S., Barnes, K. A., Church, J. A., ... Petersen, S. E. (2011). Functional network organization of the human brain. *Neuron*, *72*, 665–678.
- Power, J. D., Schlaggar, B. L., Lessov-Schlaggar, C. N., & Petersen, S. E. (2013). Evidence for hubs in human functional brain networks. *Neuron*, *79*, 798–813.

- Qing, Z., Dong, Z., Li, S., Zang, Y., & Liu, D. (2015). Global signal regression has complex effects on regional homogeneity of resting state fMRI signal. *Magnetic Resonance Imaging*, *33*, 1306–1313.
- Que, X., Checconi, F., Petrini, F., & Gunnels, J. A. (2015). Scalable community detection with the Louvain algorithm. 25–29 May 2015. pp. 28–37.
- Rubinov, M., & Sporns, O. (2010). Complex network measures of brain connectivity: Uses and interpretations. *NeuroImage*, *52*, 1059–1069.
- Saad, Z. S., Gotts, S. J., Murphy, K., Chen, G., Jo, H. J., Martin, A., & Cox, R. W. (2012). Trouble at rest: How correlation patterns and group differences become distorted after global signal regression. *Brain Connectivity*, *2*, 25–32.
- Salvador, R., Suckling, J., Coleman, M. R., Pickard, J. D., Menon, D., & Bullmore, E. (2005). Neurophysiological architecture of functional magnetic resonance images of human brain. *Cerebral Cortex*, *15*, 1332–1342.
- Schwarz, A. J., & McGonigle, J. (2011). Negative edges and soft thresholding in complex network analysis of resting state functional connectivity data. *NeuroImage*, *55*, 1132–1146.
- Sporns, O., & Betzel, R. F. (2016). Modular brain networks. *Annual Review of Psychology*, *67*, 613–640.
- Sporns, O., Tononi, G., & Kotter, R. (2005). The human connectome: A structural description of the human brain. *PLoS Computational Biology*, *1*, e42.
- Sriram, A., Gautham, K., Kothapalli, K., Narayan, P., & Govindarajulu, R. (2009). Evaluating centrality metrics in real-world networks on GPU.
- Stam, C. J. (2014). Modern network science of neurological disorders. *Nature Reviews. Neuroscience*, *15*, 683–695.
- Tian, L., Wang, J., Yan, C., & He, Y. (2011). Hemisphere- and gender-related differences in small-world brain networks: A resting-state functional MRI study. *NeuroImage*, *54*, 191–202.
- Tomasi, D., Shokri-Kojori, E., & Volkow, N. (2016). Temporal changes in local functional connectivity density reflect the temporal variability of the amplitude of low frequency fluctuations in gray matter. *PLoS One*, *11*, e0154407.
- Tomasi, D., & Volkow, N. D. (2012). Gender differences in brain functional connectivity density. *Human Brain Mapping*, *33*, 849–860.
- Turner, B. M., Paradiso, S., Marvel, C. L., Pierson, R., Boles Ponto, L. L., Hichwa, R. D., & Robinson, R. G. (2007). The cerebellum and emotional experience. *Neuropsychologia*, *45*, 1331–1341.
- Tzourio-Mazoyer, N., Landeau, B., Papathanassiou, D., Crivello, F., Etard, O., Delcroix, N., ... Joliot, M. (2002). Automated anatomical labeling of activations in SPM using a macroscopic anatomical parcellation of the MNI MRI single-subject brain. *NeuroImage*, *15*, 273–289.
- Uono, S., Sato, W., Kochiyama, T., Kubota, Y., Sawada, R., Yoshimura, S., & Toichi, M. (2017). Time course of gamma-band oscillation associated with face processing in the inferior occipital gyrus and fusiform gyrus: A combined fMRI and MEG study. *Human Brain Mapping*, *38*, 2067–2079.
- van den Heuvel, M. P., & Sporns, O. (2013). Network hubs in the human brain. *Trends in Cognitive Sciences*, *17*, 683–696.
- van den Heuvel, M. P., Stam, C. J., Boersma, M., & Hulshoff Pol, H. E. (2008). Small-world and scale-free organization of voxel-based resting-state functional connectivity in the human brain. *NeuroImage*, *43*, 528–539.
- Van Essen, D. C., Ugurbil, K., Auerbach, E., Barch, D., Behrens, T. E., Bucholz, R., ... Consortium, W. U.-M. H. (2012). The Human Connectome Project: A data acquisition perspective. *NeuroImage*, *62*, 2222–2231.
- Wang, J., Wang, X., Xia, M., Liao, X., Evans, A., & He, Y. (2015). GREYNA: A graph theoretical network analysis toolbox for imaging connectomics. *Frontiers in Human Neuroscience*, *9*, 386.
- Wang, J. H., Zuo, X. N., Gohel, S., Milham, M. P., Biswal, B. B., & He, Y. (2011). Graph theoretical analysis of functional brain networks: Test-retest evaluation on short- and long-term resting-state functional MRI data. *PLoS One*, *6*, e21976.
- Wang, Y., Du, H., Xia, M., Ren, L., Xu, M., Xie, T., ... He, Y. (2013). A hybrid CPU-GPU accelerated framework for fast mapping of high-resolution human brain connectome. *Plos One*, *8*, e62789.
- Whitfieldgabrieli, S., & Nietocastanon, A. (2012). Conn: A functional connectivity toolbox for correlated and anticorrelated brain networks. *Brain Connectivity*, *2*, 125–141.
- Williams, S., Olike, L., Vuduc, R., Shalf, J., Yelick, K., & Demmel, J. (2009). Optimization of sparse matrix-vector multiplication on emerging multicore platforms. *Parallel Computing*, *35*, 178–194.
- Wu, K., Taki, Y., Sato, K., Hashizume, H., Sassa, Y., Takeuchi, H., ... Li, X. (2013). Topological organization of functional brain networks in healthy children: Differences in relation to age, sex, and intelligence. *PLoS One*, *8*, e55347.
- Xia, M., & He, Y. (2011). Magnetic resonance imaging and graph theoretical analysis of complex brain networks in neuropsychiatric disorders. *Brain Connectivity*, *1*, 349–365.
- Xia, M., & He, Y. (2017). Functional connectomics from a “big data” perspective. *NeuroImage*, *160*, 152–167.
- Xia, M., Wang, J., & He, Y. (2013). BrainNet Viewer: A network visualization tool for human brain connectomics. *PLoS One*, *8*, e68910.
- Xu, M., Zhang, X., Wang, Y., Ren, L., Wen, Z., Xu, Y., ... Yang, H. (2012). Probabilistic brain fiber tractography on GPUs. In: IEEE. pp. 742–751.
- Yan, C., & Zang, Y. (2010). DPARSF: A MATLAB toolbox for “Pipeline” data analysis of resting-state fMRI. *Frontiers in Systems Neuroscience*, *4*, 13.
- Zhao, K., Du, H., & Wang, Y. (2017). A GPU-accelerated framework for fast mapping of dense functional connectomes. In: 2017 July 23. Nice, France. pp. 8–13.
- Zuo, X. N., Ehmke, R., Mennes, M., Imperati, D., Castellanos, F. X., Sporns, O., & Milham, M. P. (2012). Network centrality in the human functional connectome. *Cerebral Cortex*, *22*, 1862–1875.
- Zuo, X. N., He, Y., Betzel, R. F., Colcombe, S., Sporns, O., & Milham, M. P. (2017). Human connectomics across the life span. *Trends in Cognitive Sciences*, *21*, 32–45.

## SUPPORTING INFORMATION

Additional Supporting Information may be found online in the supporting information tab for this article.

**How to cite this article:** Du H, Xia M, Zhao K, et al. PAGANI Toolkit: Parallel graph-theoretical analysis package for brain network big data. *Hum Brain Mapp*. 2018;00:1–17. <https://doi.org/10.1002/hbm.23996>